RESEARCH ARTICLE

Direct Power Control of a Surface-Mounted Permanent Magnet Synchronous Generator Wind Turbine for Offshore Applications

CHIKEZIE M. EMEGHARA, (Student Member, IEEE),
SATISH M. MAHAJAN, (Life Senior Member, IEEE),
AND ALI ARZANI, (Member, IEEE)
Center for Energy Systems Research (CESR), Tennessee Technological University, Cookeville, TN 38505, USA

Corresponding author: Chikezie M. Emeghara (cmemeghara42@tntech.edu)

ABSTRACT This paper proposes a direct power control scheme for an offshore wind turbine-driven surface-mounted permanent magnet synchronous generator with a full back-to-back converter situated onshore to decentralize the weight of the turbine. The proposed model is designed in a stationary reference frame and does not require a phase-locked loop as opposed to the traditional vector current control method. Simple feed-forward and feedback control loops are used in the proposed model to extract the maximum available wind power, maintain constant voltage at the coupling DC link, and ensure power injection into the electric network at unity power factor. Simulation results carried out in MATLAB/SIMULINK show that the proposed model has a fast transient response and steady-state performance consistent with the vector current control model. Furthermore, eigenvalue analysis results demonstrate that the proposed method's performance is robust to variations in different system parasitic elements, even under both stiff and weak electric network conditions. These results also indicate that the back-to-back converter can operate effectively when located onshore close to the load center while the turbine is in close proximity offshore. This can be suitable for multiple specific offshore applications as it can potentially reduce the overall weight, volume, and cost of the offshore wind turbine infrastructure.

INDEX TERMS Back-to-back converter, direct power control, surface-mounted permanent magnet synchronous generator, short-circuit ratio, weak electric networks.

NOMENCLATURE
ABBREVIATIONS

BTB	Back-to-back.
DFIG	Doubly-fed induction generator.
GSC	Grid-side converter.
MPPT	Maximum power point tracking.
MSC	Machine-side converter.
OWT	Offshore wind turbine.
PCC	Point of common coupling.
PLL	Phase-locked loop.
PMSG	Permanent magnet synchronous generator.
SCR	Short-circuit ratio.
SPMSG	Surface-mounted permanent magnet synchronous generator.
VCC	Vector current control.

SUBSCRIPTS

1, 2	MSC and GSC components, respectively.
dc	DC link component.
$g\alpha\beta$	GSC components in rotating stationary reference frame.
MPP	Maximum power point.
P, Q	Active and reactive power term.
$r\alpha\beta$	SPMSG rotor components in rotating stationary reference frame.

The associate editor coordinating the review of this manuscript and approving it for publication was Chandan Kumar.

$s\alpha\beta$	SPMSG stator components in rotating stationary reference frame.
s, r	SPMSG stator and rotor components.
ω	Average wind speed component.

SUPERSCRIPT

$*$	reference.

VARIABLES & SYMBOLS

A	Cross-sectional area of the wind turbine blade [m^2].
C_{dc}	DC link capacitance [F].
$C_p(\lambda, \beta)$	Efficiency of power extraction.
p	Differential operator, $\left(p = \frac{d}{dt}\right)$.
P	Number of poles.
P_g, Q_g	Electric network active [W] and reactive power [VAR].
P_s, Q_s	SPMSG active [W] and reactive power [VAR].
P_t	Turbine mechanical power (W).
$i_{g\alpha\beta}$	GSG current [A] in stationary reference frame.
$i_{s\alpha\beta}, i_{r\alpha\beta}$	SPMSG stator and rotor current [A].
J	Inertia constant [$kg.m^2$].
$M_{s\alpha\beta}, M_{g\alpha\beta}$	MSC and GSC modulation index.
R	Turbine blade radius [m].
R_1, L_1	Line resistance [Ω] and inductance [H] connecting the SPMSG to the MSC.
R_g, L_g	Electric network line resistance [Ω] and inductance [H], respectively.
R_s, L_s	SPMSG resistance [Ω] and inductance [H].
s	Slip.
S_g	Complex power injected into electric network [VA].
S_s	SPMSG stator complex power [VA].
T_e	Electromagnetic torque [N.m].
T_t	Torque developed by the turbine shaft [N.m].
U_{sP}, U_{sQ}	Instantaneous stator active and reactive power input components.
U_{gP}, U_{gQ}	Instantaneous GSC active and reactive power input components.
$v_{1\alpha\beta}$	MSC input voltage [V].
$v_{2\alpha\beta}$	GSC output voltage [V].
v_{dc}	DC link voltage [V].
$v_{g\alpha\beta}$	Electric network voltage [V].
$v_{pcc,nom}$	PCC nominal voltage [V].
$v_{s\alpha\beta}, v_{r\alpha\beta}$	SPMSG stator and rotor voltage [V].
V_w	Average wind speed [m/s].
w_e	Electric network angular frequency [rad/s].
w_r	Rotor speed [rpm].
w_t	Angular speed of the turbine [rpm].
Z_g	Electric network impedance [Ω].
α	PI controller bandwidth [Hz].
β	Turbine blade pitch angle [°].
λ	Tip speed ratio (TSR).

λ_m	Magnet flux linkage [Wb].
$\lambda_{r\alpha\beta}, \lambda_{s\alpha\beta}$	SPMSG rotor and stator flux linkage [Wb], respectively.
ρ	Air density [kg/m^3].

I. INTRODUCTION

Wind power stations face challenges due to the high volume and weight of their components [1], which can result in elevated installation and maintenance costs, particularly for offshore wind power stations. As a result, researchers and engineers are exploring new approaches to address these challenges. One approach that has gained attention is the OWT. OWTs offer several advantages over onshore turbines, including the ability to be deployed in deeper waters, providing access to stronger and more consistent winds, resulting in higher energy production and lower costs per unit of energy [1], [2], [3]. OWTs, particularly the floating type, also offer greater flexibility in site selection and can be relocated to different locations as needed [4]. This feature can help reduce potential conflicts with other ocean uses.

The choice of generator for an OWT can impact its performance, including factors such as efficiency, power quality, cost, and reliability. The most popular types of electric generators used for wind power generation are the squirrel cage induction generator, DFIG, and PMSG. Of these types, PMSGs are widely used due to their high efficiency, reliability, power density, and lower acoustical noise [5], [6], [7]. The authors in [8] proposed a hybrid HVDC converter connected DFIG wind farm to reduce the overall weight and cost of offshore wind power stations, but the analysis provided little information on the system stability, which is essential for performance viability checks. Although the DFIG can be used as a source of active and reactive power to the electric network with a converter rating of one-third of the machine rating, PMSG has no rotor copper loss and requires no excitation [9].

In this paper, the focus is on SPMSG-based wind turbines due to their decreased risk of demagnetization, cost-effective manufacturing, enhanced cooling capabilities, and adaptability to high-speed operations [10], [11]. In SPMSGs, the direct-axis and quadrature-axis inductances are the same. Consequently, SPMSGs do not produce substantial reluctance torque. The low flux leakage in these generators streamlines the design process, eliminating the need for intricate magnetic shielding, compensation, or control strategies commonly required in interior permanent magnet machines with unequal direct-axis and quadrature-axis inductances [12]. These features contribute to superior system performance compared to other PMSG alternatives.

Typically, the SPMSG rotor is directly coupled to the turbine, while the stator connects to the electric network via a full BTB-converter, consisting of an MSC, DC link, and GSC. Conventional MSCs utilize inner-current and outer-speed PI control loops, whereas GSCs employ inner-current and outer-voltage PI control loops [5], [9], [13], [14]. Voltage-oriented control (VOC) and direct-power control techniques

are widely adopted for GSC implementation [15], while field-oriented control (FOC) and direct-torque control (DTC) techniques are suitable for MSC [16]. To enhance the performance of PMSG-electric network integration, various advanced control schemes have been introduced, including fuzzy logic control [5], [17], [18], [19] and predictive control [9], [20]. Although both techniques can be easily adapted for nonlinear dynamic systems, the predictive approach entails computational complexities, particularly for multilevel converters. In contrast, the fuzzy logic controller may struggle to handle nonlinear variables with a high degree of uncertainty.

To achieve optimal control of PMSG, [21] proposed a vector current control (VCC) method for maximum wind power electric network injection. The VCC model is designed in a synchronous rotating reference frame and requires a phase-locked loop (PLL) system. One major disadvantage of the VCC method is its susceptibility to slow transient response due to the dependence on PLL [22]. Moreover, the interaction between the PLL and current loop control systems may cause power quality issues [23], [24]. For improved transient performance, the direct power control technique has emerged as a superior alternative to PLL-based control methods. In [25], a sliding mode control technique was proposed for DPC to achieve effective power control with improved transient performance and low sensitivity to parameter mismatch. However, this approach is susceptible to the chattering phenomenon. In an effort to improve DPC, [26] introduced a grid voltage-modulated DPC technique to achieve fast convergence of instantaneous active and reactive power control with reduced ripples and total harmonic distortion. It is worth noting, however, that this technique is highly dependent on the system parameters [27].

While the concept of DPC has been extensively studied in [22], [25], [26], [27], and [28], there is limited information available on the model dynamics coupling of MSC and GSC, as well as their performance under weak electric network conditions. This paper introduces a DPC technique for effective kW-scale OWT-SPMSG power injection into the electric network. The OWT connects to the electric network through a full back-to-back converter situated at the central onshore substation, where other power conditioning equipment is housed or within the deck of a rig platform. This configuration helps reduce the overall weight of the turbine. One might argue that relocating the converter from the wind turbine to the substation may not result in significant savings. Nonetheless, it is crucial to recognize that the converter weight, accounting for a part of the aerodynamic load on the turbine infrastructure, is relocated to a stationary platform, resulting in OWT structural infrastructure savings. By removing this weight from the turbine platform, it is expected that the required reinforcement for the OWT's infrastructure will reduce.

In this paper, the dynamics of the proposed MSC, GSC, and coupling DC link are evaluated and compared with the conventional VCC. The key contribution of this paper is the introduction of an effective DPC scheme for the OWT-SPMSG system. Some of the significant highlights of this paper include:

- The proposed DPC scheme for the OWT-SPMSG system does not require complex calculations for the reference current or fine-tuned inner current control loops. The proposed scheme eliminates the need for sequential decomposition in power control loops instead of the traditional VCC approach. It also does not require using PLL, which has several limitations, including sensitivity to phase noise, loop stability issues, limited bandwidth, and lock-time delay problems that can reduce the system's performance and accuracy.
- The time-domain and eigenvalue analyses confirm the OWT-SPMSG system's robust performance to variations of different system parasitic elements, especially under weak electric network conditions.
- The proposed scheme allows the BTB-converter to be located onshore close to the load center while the turbine is offshore near the BTB-converter. This makes it desirable for multiple specific offshore applications since it will have the potential to reduce the overall weight, volume, and cost of OWT infrastructure.

The paper is organized into the following sections: Section II describes the offshore applications of the proposed DPC OWT-SPMSG system. Section III shows the system models, including the wind turbine, SPMSG and MSC, GSC, and the DC link. In section IV, the design of the direct power controller is presented. Section V presents the stability analysis of the OWT-SPMSG system. Section VI shows the simulation results of the system under study, followed by a discussion of the results. Finally, Section VII provides the concluding remarks of this research.

II. OFFSHORE APPLICATIONS

The proposed offshore kW-scale wind turbine has the potential to be an eco-friendly and cost-effective energy source for various applications, particularly when combined with supplementary energy sources such as solar, battery banks, or diesel generators. Some of these offshore applications are suggested in the following subsections.

A. SEAWATER DESALINATION PLANTS

These plants are designed to transform impure and saline seawater into potable water for both onshore and offshore use. Traditionally, these plants rely on electric network power (for stationary onshore plants) or fossil-based energy sources (for mobile offshore plants). In the latter scenario, with the growing adoption of offshore wind energy, replacing fossil-based energy sources in commissioned plants with wind power can offer a cost-effective alternative. In 2021, SYNLIFT Industrial Products unveiled plans to install a Floating WINDdesal (FWD), an innovative offshore seawater desalination plant concept primarily powered by a wind turbine mounted on the same semi-submersible offshore structure [29].
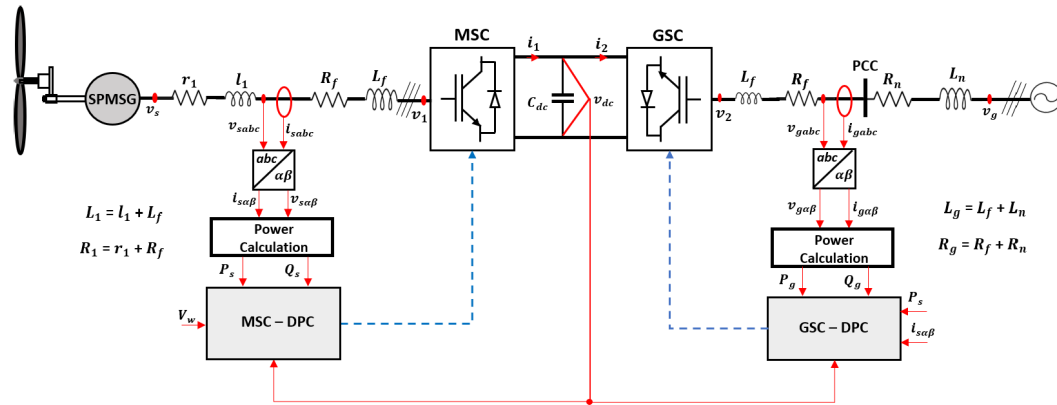
FIGURE 1. Schematic diagram of the proposed direct power controlled SPMSG-electric network system.
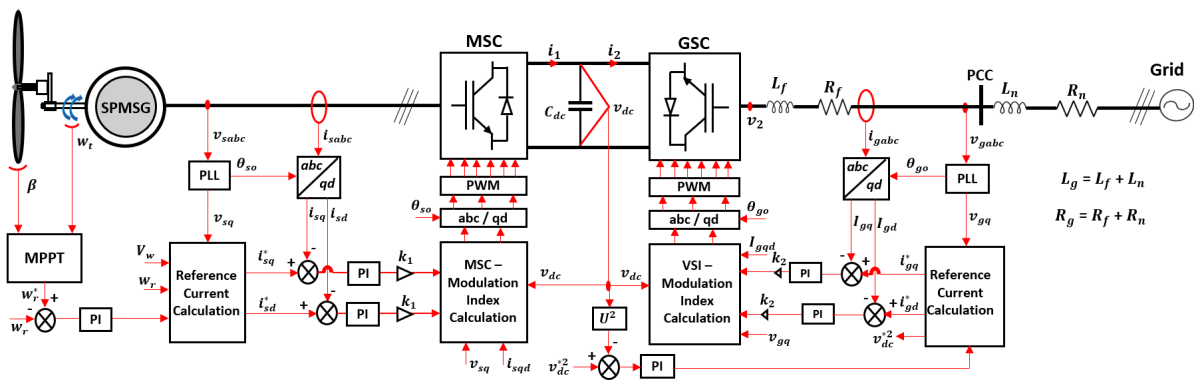

FIGURE 2. Traditional VCC block diagram for electric network connected SPMSG wind turbine.

However, this technology is still emerging, and the structures of previously commissioned plants may not be able to support the weight or structural dynamics (e.g., aerodynamic loads on the blades) of a large wind turbine during operation without installing a new floating structure. Moreover, the plant structure might not have sufficient space to accommodate multiple smaller wind turbines. In this situation, several offshore kW-scale SPMSG wind turbines positioned nearby can be integrated to power these off-grid desalination plants. For each kW-scale PMSG wind turbine, its BTB-converter and control unit can be housed in cabinets located in the desalination plant facility.

B. OIL AND GAS RIGS

Offshore rig platforms typically have MW-scale energy requirements, primarily supplied by fossil-based generation, such as diesel and gas generators. Recently, MW-scale floating wind turbines have been under development in Norway to power offshore oil and gas rigs [30]. Commercial 3-6 kW PMSG wind turbines have also been employed to power low voltage and industrial equipment (48V-300V) on unmanned oil and gas platforms [31]. However, higher kW ratings necessitate more space for installing the wind energy conversion system.

With the proposed DPC OWT-SPMSG system presented in this paper, within confined deck spaces, the BTB-converter cabinet and controls can be installed in one location, and the wind turbine can be optimally placed on the deck. This arrangement can be suitable for already commissioned offshore platforms with limited deck space, such as oil and gas rigs and offshore green hydrogen production plants.

III. SYSTEM MODELING

The model presented in Fig. 1 illustrates the schematic diagram of a direct power-controlled OWT-SPMSG using a full back-to-back converter. The effectiveness of the proposed MSC-DPC and GSC-DPC controllers are evaluated by comparing them with the conventional VCC scheme, as modeled in [22], [32], and [33] and depicted in Fig. 2. Specifically, the performance of the MSC-DPC and GSC-DPC control blocks shown in Fig. 1 are evaluated and compared to the traditional VCC topology to determine whether the proposed control model can outperform the conventional approach or offer any additional benefits in terms of control system performance.

Additionally, this section analyzes the mathematical model of the proposed system in Fig. 1. The system components are evaluated to understand how the model directly controls the captured wind power and ensures proper power injection

TABLE 1. System parameters.

Wind Turbine Parameters			
P_t	30 kW	n_r	6
R	6 m	β	$0°$
$V_{w-rated}$	10 m/s	ρ	$1.225 kg/m^3$
SPMSG, DC Link and electric network Parameters			
v_s	460 V	R_s	0.0651 Ω
i_s	65 A	$L_{\alpha s}$	9.1 mH
w_r	720 rpm	$L_{\beta s}$	9.1 mH
P (no of pole pairs)	6	L_1	0.349326 mH
λ_m	0.09	R_1	30.324 mΩ
v_{dc}	900 V	C_{dc}	10 mF
v_g	380∠0°	ω_e	377 rad/s
R_g	0.179056 Ω	L_g	1.553581 mH

into the electric network. The system architecture includes an OWT, SPMSG, MSC, GSC, and short-distance electric lines. The OWT drives the SPMSG rotor to convert the energy captured by the turbine into electrical energy. The SPMSG output is connected to the electric network through R_1, L_1 and a full back-to-back converter, which consists of the MSC (AC/DC) and GSC (DC/AC).

In this paper, R_1 and L_1 represents the short-distance line connecting the offshore SPMSG to the onshore converter station, primarily to reduce the overall weight of the OWT. the MSC-DPC is modeled to control the SPMSG rotor speed and obtain the maximum available power for every change in wind speed. The GSC controls active and reactive power injection/absorption into the electric network. It also ensures near-constant DC link voltage control. The GSC output is connected to the electric network through R_g and L_g. Table 1 presents the wind turbine, SPMSG, and electric network parameters used in this study.

A. WIND TURBINE MODELING
The extractable mechanical power from a given OWT can be deduced with the following relation [7], [21], [34]:

$$P_t = 0.5 * \rho A C_P(\lambda, \beta) V_w^3 \qquad (1)$$

$$T_t = \frac{P_t}{w_t} = \frac{0.5}{w_t} \rho A C_P(\lambda, \beta) V_w^3 \qquad (2)$$

$$C_P(\lambda, \beta) = 0.73[\frac{151}{\lambda_i} - 0.58\beta - 0.002\beta^{2.14} - 13.2]e^{\frac{-18.4}{\lambda_i}} \qquad (3)$$

$$\frac{1}{\lambda_i} = \frac{1}{\lambda - 0.02\beta} - \frac{0.003}{\beta^3 + 1} \qquad (4)$$

$$\lambda = \frac{w_t R}{V_w} \qquad (5)$$

Fig. 3 shows that the operating range of any given wind turbine is characterized by a unique pitch angle irrespective of change in wind speed [9], [21]. This entails that the amount of maximum extractable power from the wind is specific to a certain average speed per operating condition.

To capture the maximum power for any wind speed [21]:

$$\frac{dP_t}{dw_r} = \frac{1}{2}\text{p}Av_w^3\frac{dC_P}{d\lambda_i} * \frac{d\lambda_i}{dw_r} = 0$$
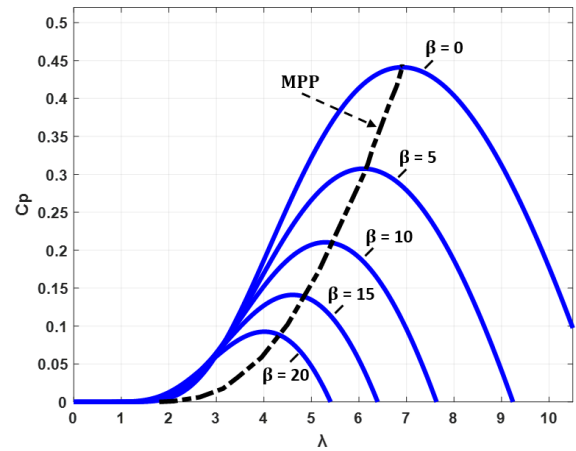
$$\implies w_{tMPP} = \frac{\lambda_{MPP}v_w}{R}$$

FIGURE 3. $C_P(\lambda, \beta) - \lambda$ response for various pitch angles.

Where $w_{rMPP} = n_{gear} * w_{tMPP}$

$$P_{tMPP} = \frac{1}{2}\text{p}AC_{PMPP}\left(\frac{\omega_{rMPP}R}{n_{gear}\lambda_{MPP}}\right)^3 \qquad (6)$$

Also, the OWT mechanical model considering wind speed and machine torque relationship is expressed as:

$$J\left(\frac{2}{P}\right)p\omega_r = T_t - T_e = \sigma_w \qquad (7)$$

B. SPMSG AND MSC MODELING
In this section, the SPMSG in Fig. 1 is analyzed in stationary reference frame ($\alpha\beta$) transformation to obtain the system's mathematical model. The stator Voltage equation when referred to $\alpha\beta$-reference frame includes:

$$v_{s\alpha} = R_s i_{s\alpha} + p\lambda_{s\alpha} + \omega_r \lambda_{s\beta} + R_1 i_{s\alpha} + L_1 p i_{s\alpha} + i_{1\alpha} \qquad (8)$$

$$v_{s\beta} = R_s i_{s\beta} + p\lambda_{s\beta} - \omega_r \lambda_{s\alpha} + R_1 i_{s\beta} + L_1 p i_{s\beta} + v_{1\beta} \qquad (9)$$

The Rotor Voltage equation when referred to $\alpha\beta$-reference frame are as follows:

$$v_{r\alpha} = R_r i_{r\alpha} + p\lambda_{r\alpha} \qquad (10)$$

$$v_{r\beta} = R_r i_{r\beta} + p\lambda_{r\beta} \qquad (11)$$

The following equation relates the SPMSG rotor and stator current:

$$\lambda_{s\alpha} = L_{s\alpha} i_{s\alpha} + L_{m\alpha} i_{r\alpha} \qquad (12)$$

$$\lambda_{s\beta} = L_{s\beta} i_{s\beta} + L_{m\beta} i_{r\beta} + \lambda_m \qquad (13)$$

$$\lambda_{r\alpha} = L_{r\alpha} i_{r\alpha} + L_{m\alpha} i_{s\alpha} \qquad (14)$$

$$\lambda_{r\beta} = L_{r\beta} i_{r\beta} + L_{m\beta} i_{s\beta} + \lambda_m \qquad (15)$$

The dynamics of the rotor of a permanent magnet machine are neglected due to poor electric conductivity [13]. Thus, $i_{r\alpha} = i_{r\beta} = 0$, substitute into (12-15):

$$\lambda_{s\alpha} = L_{s\alpha} i_{s\alpha} \qquad (16)$$

$$\lambda_{s\beta} = L_{s\alpha} i_{s\alpha} + \lambda_m \qquad (17)$$

Substitute (16-17) into (8-9), respectively.

$v_{s\alpha} = R_s i_{s\alpha} + L_{s\alpha} p i_{s\alpha} + \omega_r(L_{s\alpha} i_{s\beta} + \lambda_m) + R_1 i_{s\alpha} + L_1 p i_{s\alpha} + v_{1\alpha}$

$v_{s\beta} = R_s i_{s\beta} + p(L_{s\beta} i_{s\alpha} + \lambda_m) - \omega_r L_{s\alpha} i_{s\alpha} + R_1 i_{s\beta} + L_1 p i_{s\beta} + v_{1\beta}$

Let, $R = R_s + R_1$, $L_s = L_{s\alpha} = L_{s\beta}$, $L = L_s + L_1$ & $p\lambda_m = 0$.

$$pi_{s\alpha} = \frac{1}{L}(v_{s\alpha} - R i_{s\alpha} - \omega_r L_s i_{s\beta} - \omega_r \lambda_m - v_{1\alpha}) \quad (18)$$

$$pi_{s\beta} = \frac{1}{L}(v_{s\beta} - R i_{s\beta} + \omega_r L_s i_{s\alpha} - v_{1\beta}) \quad (19)$$

Since stator complex power is given:

$$S_s = P_s + jQ_s = \frac{3}{2} v_s i_s^* = \frac{3}{2}(v_{s\alpha} + jv_{s\beta}) * (i_{s\alpha} - ji_{s\beta}),$$

the instantaneous power generated in the SPMSG can be deduced by simply taking the derivative of "S_s", thus:

$$pP_s = \frac{3}{2}[v_{s\alpha} pi_{s\alpha} + i_{s\alpha} pv_{s\alpha} + v_{s\beta} pi_{s\beta} + i_{s\beta} pv_{s\beta}] \quad (20)$$

$$pQ_s = \frac{3}{2}[-v_{s\alpha} pi_{s\beta} - i_{s\beta} pv_{s\alpha} + v_{s\beta} pi_{s\alpha} + i_{s\alpha} pv_{s\beta}] \quad (21)$$

Assume that the SPMSG in Fig. 1 is connected to an ideal electric network with angular frequency, ω_e, the stator voltage referred to $\alpha\beta$ reference frame can be given as: $v_{s\alpha} = v_s cos(s\omega_e + \delta)$ and $v_{s\beta} = -v_s sin(s\omega_e + \delta)$, thus, the decoupled instantaneous stator voltages are as follows:

$$pv_{s\alpha} = s\omega_e v_{s\beta} \quad (22)$$

$$pv_{s\beta} = -s\omega_e v_{s\alpha} \quad (23)$$

By Substituting (18-19) and (22-23) into (20), instantaneous active power delivered by the stator can be obtained:

$$pP_s = -\frac{R}{L}P_s + \left(\frac{\omega_r L_s}{L} + s\omega_e\right)Q_s + \frac{3}{2L}(v_s^2 - v_{1\alpha} v_{s\alpha} - v_{1\beta} v_{s\beta} - \omega_r \lambda_m V_{s\alpha}) \quad (24)$$

where $v_s^2 = v_{s\alpha}^2 + v_{s\beta}^2$

From (24), let the SPMSG time-invariant active power input function be represented as:

$$U_{sP} = v_s^2 - v_{1\alpha} v_{s\alpha} - v_{1\beta} v_{s\beta} - \omega_r \lambda_m V_{s\alpha} \quad (25)$$

Substitute (25) into (24):

$$\Rightarrow U_{sP} = \frac{2L}{3}\left[\left(p + \frac{R}{L}\right)P_s - \left(\frac{\omega_r L_s}{L} + s\omega_e\right)Q_s\right],$$

let:

$$\sigma_{Ps} = \left(p + \frac{R}{L}\right)P_s \quad (26)$$

And, $k_1 = \frac{2L}{3}$ and $k_2 = \left(\frac{\omega_r L_s}{L} + s\omega_e\right)$

$$\therefore U_{sP} = k_1 \sigma_{Ps} - k_1 k_2 Q_s \quad (27)$$

To obtain the instantaneous reactive power delivered by the stator, substitute (18-19) and (22-23) into (21):

$$pQ_s = -\frac{R}{L}Q_s - \left(\frac{\omega_r L_s}{L} + s\omega_e\right)P_s - \frac{3}{2L}(-v_{s\alpha} v_{1\beta} + v_{s\beta} v_{1\alpha} + \omega_r \lambda_m V_{s\beta}) \quad (28)$$

From (28), let the instantaneous stator reactive power input be:

$$U_{sQ} = -v_{s\alpha} v_{1\beta} + v_{s\beta} v_{1\alpha} + \omega_r \lambda_m V_{s\beta}$$

$$\Rightarrow U_{sQ} = \frac{2L}{3}\left[-\left(p + \frac{R}{L}\right)Q_s - \left(\frac{\omega_r L_s}{L} + s\omega_e\right)P_s\right], \quad (29)$$

let:

$$\sigma_{Qs} = \left(p + \frac{R}{L}\right)Q_s \quad (30)$$

$$\therefore U_{sQ} = -k_1 \sigma_{Qs} - k_1 k_2 P_s \quad (31)$$

Solving (25) & (29) simultaneously, the input voltage to the MSC is deduced as follows:

$$v_{1\alpha} = \frac{v_s^2(v_{s\alpha} - \omega_r \lambda_m) - U_{sP} v_{s\alpha} + U_{sQ} V_{s\beta}}{v_s^2} \quad (32)$$

$$v_{1\beta} = \frac{v_s^2 v_{s\beta} - U_{sP} v_{s\beta} - U_{sQ} V_{s\alpha}}{v_s^2} \quad (33)$$

C. GSC MODELING

The dynamic model of the GSC, when referred to the stationary reference frame, is deduced in this section. From Fig. 1, the following GSC output voltage can be deduced:

$$pi_{g\alpha\beta} = \frac{v_{2\alpha\beta}}{L_g} - \frac{R_g}{L_g} i_{g\alpha\beta} - \frac{v_{g\alpha\beta}}{L_g} \quad (34)$$

Assume an ideal network, the electric network voltage in $\alpha\beta$-reference frame includes [14], [15]:

$$\Rightarrow v_{g\alpha\beta} = |v_g|[cos(\omega_e + \theta_0) - jsin(\omega_e + \theta_0)]$$

$$\therefore pv_{g\alpha\beta} = \omega_e v_{g\beta} - j\omega_e v_{g\alpha} \quad (35)$$

Also, $S_g = \frac{3}{2} v_{g\alpha\beta} i_{g\alpha\beta}^*$

By differentiating S_g and substituting (30) and (31), the instantaneous complex power model is obtained as follows:

$$pS_g = \frac{3}{2L_g}\left(v_{2\alpha} v_{g\alpha} + v_{2\beta} v_{g\beta} - |v_g|^2\right) - \frac{R_g}{L_g}P_g + \omega_e Q_g$$
$$+ j\left[\frac{3}{2L_g}(v_{2\alpha} v_{g\beta} + v_{2\beta} v_{g\alpha}) - \frac{R_g}{L_g}Q_g - \omega_e P_g\right] \quad (36)$$

From (36), let the GSC inputs for active and reactive power include the following:

$$U_{pg} = v_{2\alpha} v_{g\alpha} + v_{2\beta} v_{g\beta} - |v_g|^2 \quad (37)$$

$$U_{Qg} = v_{2\alpha} v_{g\beta} - v_{2\beta} v_{g\alpha} \quad (38)$$

Substitute (37-38) into (36) and decouple the complex power:

$$\Rightarrow U_{Pg} = \frac{2L_g}{3}\left[\left(p + \frac{R_g}{L_g}\right)P_g - \omega_e Q_g\right]$$

And, $U_{Qg} = \frac{2L_g}{3}\left[\left(p + \frac{R_g}{L_g}\right)Q_g + \omega_e P_g\right]$, let:

$$\sigma_{Pg} = \left(p + \frac{R_g}{L_g}\right)P_g \quad (39)$$

$$\sigma_{Qg} = \left(p + \frac{R_g}{L_g}\right)Q_g \quad (40)$$
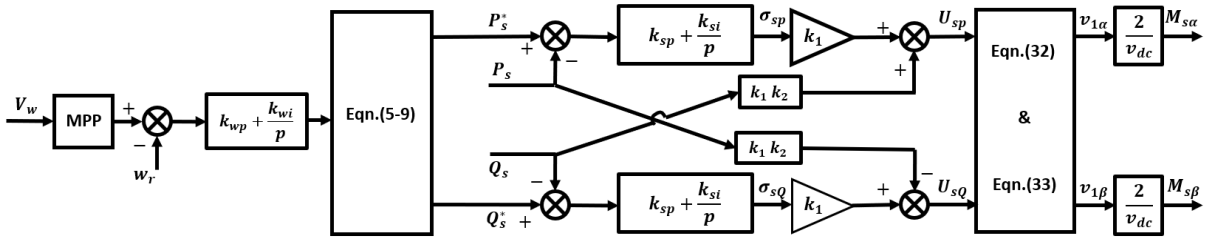
FIGURE 4. MSC-DPC controller design for optimal wind speed and stator power regulation.

And,

$$k_g = \frac{2L_g}{3}$$

$$\therefore U_{Pg} = k_g\sigma_{Pg} - k_g\omega_e Q_g$$

$$\therefore U_{Qg} = k_g\sigma_{Qg} + k_g\omega_e P_g$$

By solving (37) and (38) simultaneously, the GSC output voltage is expressed as:

$$v_{2\beta} = \frac{U_{pg}v_{g\beta} - U_{Qg}v_{g\alpha}}{|v_g|^2} + v_{g\beta} \tag{41}$$

$$v_{2\alpha} = \frac{U_{pg}v_{g\alpha} + U_{Qg}v_{g\beta}}{|v_g|^2} + v_{g\alpha} \tag{42}$$

D. DC LINK DYNAMIC MODELING

From Fig. 1 the model for the DC link constant voltage control is deduced as follows:

$$C_{dc}pv_{dc} = -\frac{3}{4}\text{Re}\left[M_{s\alpha\beta}i_{s\alpha\beta} + M_{\alpha\beta g}i_{g\alpha\beta}\right] \tag{43}$$

By multiplying both sides of (43) by v_{dc}, the dc link voltage is obtained in terms of converter active power and evaluating the following converter voltage and modulation index relation, $v_{1\alpha\beta} = \frac{M_{\alpha\beta s}}{2}v_{dc}$ and $v_{2\alpha\beta} = \frac{M_{\alpha\beta g}}{2}v_{dc}$, implies:

$$\frac{C_{dc}}{2}pv_{dc}^2 = -\frac{3}{2}\text{Re}\left[v_{S\alpha\beta}i_{S\alpha\beta} + v_{g\alpha\beta}i_{g\alpha\beta}\right] = -(P_s + P_g) \tag{44}$$

IV. CONTROLLER DESIGN
A. MSC CONTROLLER DESIGN

In this section, the objective is to design a PI-based controller to extract the maximum available power from the wind by controlling the rotor speed and assuming a 0° pitch angle. The MSC controller in Fig. 4 is designed to transfer the maximum available power from the SPMSG to the electric network. The instantaneous speed, subject to (7), is used to obtain the maximum power induced in the stator and is used as a reference for MPPT. For speed controller design using PI, from (7) let,

$$\sigma_w = k_w\left(w_r^* - w_r\right) = J\left(\frac{2}{P}\right)p\omega_r \tag{45}$$

where k_w is the PI controller gain.

By manipulating (45), the SPMSG rotor speed transfer functional model is determined:

$$\Rightarrow \frac{w_r}{w_r^*} = \frac{\frac{Pk_w}{2J}}{p + \frac{Pk_w}{2J}} \tag{46}$$

From (46), poles $= -\frac{Pk_w}{2J}$. Thus, let,

$$\alpha = \frac{Pk_w}{2J} \Rightarrow k_w \equiv \frac{2\alpha J}{P} \tag{47}$$

where, $k_w = k_{wp} + \frac{k_{wi}}{p}$ and $p = \frac{d}{dt}$

The PI controller integral and proportional gains for the rotor speed controller are determined by manipulating (46-47):

$$\therefore k_{wp} = \frac{2\alpha J}{P} \quad \& \quad k_{wi} = 0$$

The decoupled stator instantaneous active and reactive power in (20) and (21) are used to design the MSC PI controllers. For MSC active power PI controller design, from (26), let,

$$\sigma_{Ps} = k_{Ps}(P_s^* - P_s) = \left(p + \frac{R}{L}\right)P_s \tag{48}$$

Manipulating (48) and deducing the transfer function model implies: $k_{Ps}P_s^* = (p + \frac{R}{L} + k_{Ps})P_s$.

Where, $k_{Ps} = k_{Psp} + \frac{k_{Psi}}{p}$ and $p = \frac{d}{dt}$

$$\Rightarrow \frac{P_s}{P_s^*} = \frac{k_{Psp} + \frac{k_{Psi}}{p}}{p + \frac{R}{L} + k_{Psp} + \frac{k_{Psi}}{p}}$$

$$= \frac{k_{Psp}\left(1 + \frac{k_{Psi}}{pk_{Psp}}\right)}{p\left(1 + \frac{R}{Lp}\right) + k_{Psp}\left(1 + \frac{k_{Psi}}{pk_{Psp}}\right)}.$$

Let,

$$\frac{R}{L} = \frac{k_{Psi}}{k_{Psp}} \tag{49}$$

$$\frac{P_s}{P_s^*} = \frac{k_{Psp}}{p + k_{Psp}} \tag{50}$$

From (50), Poles $= -k_{Psp}$. Let the bandwidth be defined as:

$$\alpha = k_{Psp} \tag{51}$$

The integral gain is obtained by substituting (51) into (49):

$$k_{Psi} = \frac{R}{L}\alpha \tag{52}$$

Also, for MSC reactive power controller design, from (30): $\sigma_{Qs} = (p + \frac{R}{L})Q_s$. Using PI controller, Let,

$$\sigma_{Qs} = k_{Qs}\left(Q_s^* - Q_s\right) = \left(p + \frac{R}{L}\right)Q_s \qquad (53)$$

where, $k_{Qs} = k_{Qsp} + \frac{k_{Qsi}}{p}$

$$\Rightarrow \frac{Q_s}{Q_s^*} = \frac{k_{Qsp} + \frac{k_{Qsi}}{p}}{p + \frac{R}{L} + k_{Qsp} + \frac{k_{Qsi}}{p}}$$

$$= \frac{k_{Qsp}\left(1 + \frac{k_{Qsi}}{pk_{Qsp}}\right)}{p\left(1 + \frac{R}{Lp}\right) + k_{Qsp}\left(1 + \frac{k_{Qsi}}{pk_{Qsp}}\right)}$$

Let

$$\frac{k_{Qsi}}{k_{Qsp}} = \frac{R}{L} \qquad (54)$$

$$\frac{Q_s}{Q_s^*} = \frac{k_{Qsp}}{p + k_{Qsp}} \qquad (55)$$

From (55), Poles = $-k_{Qsp}$. Bandwidth is defined as:

$$\alpha = k_{Qsp} \qquad (56)$$

The integral gain is obtained by substituting (56) into (54):

$$k_{Qsi} = \frac{R}{L}\alpha \qquad (57)$$

B. GSC CONTROLLER DESIGN

The purpose of the GSC in this paper is to regulate the dc link voltage level and inject power into the electric network. Fig. 5 depicts the designed GSC controller, which utilizes PI controllers and feedforward control loops. One PI controller is designed to maintain the dc link voltage magnitude close to constant, while a combination of PI and feedforward loop control is used for the decoupled active and reactive power control. Manipulating (36-38):

$$\Rightarrow pP_g = \omega_e Q_g - \frac{R_g}{L_g}P_g + \frac{3}{2L_g}U_{pg}$$

$$\Rightarrow U_{pg} = \frac{2L_g}{3}\left(\frac{dP_g}{dt} + \frac{R_g}{L_g}P_g\right) - \frac{2L_g}{3}\omega_e Q_g$$

$$k_{gp} = \frac{2L_g}{3}$$

$$\Rightarrow U_{pg} = -K\omega_e Q_g + K\left[\frac{dP_g}{dt} + \frac{R_g}{L_g}P_g\right]$$

$$\Rightarrow \sigma_{Pg} = \frac{dP_g}{dt} + \frac{R_g}{L_g}P_g = k_{gp}\left(P_g^* - P_g\right)$$

$$\Rightarrow k_{gp}P_g^* = \left(\frac{d}{dt} + \frac{R_g}{L_g} + k_{gp}\right)P_g$$

$$\Rightarrow \frac{P_g}{P_g^*} = \frac{k_{gp}}{\frac{d}{dt} + \frac{R_g}{L_g} + k_{gp}} = \frac{k_{gpp} + \frac{k_{gpi}}{p}}{p + \frac{R_g}{L_g} + k_{gpp} + \frac{k_{gpi}}{p}}$$

$$\Rightarrow \frac{P_g}{P_g^*} = \frac{k_{gpp}\left(1 + \frac{k_{gpi}}{pk_{gpp}}\right)}{p\left(1 + \frac{R_g}{pL_g}\right) + k_{gpp}\left(1 + \frac{k_{gpi}}{pk_{gpp}}\right)} \qquad (58)$$

Let

$$\frac{R_g}{\rho L_g} = \frac{k_{gpi}}{\rho k_{gpp}} \rightarrow k_{gpi} = \frac{R_g}{\rho L_g}k_{gpp}$$

$$\frac{P_g}{P_g^*} = \frac{k_{gpp}}{p + k_{gpp}}$$

$$pole = -k_{gpp}\alpha = k_{gpp} \text{ (bandwidth)}$$

$$\therefore k_{gpi} = \frac{R_g}{L_g}\alpha k_{gpp} = \alpha \qquad (59)$$

The electric network reactive component from (36):

$$\Rightarrow \frac{dQ_g}{dt} = -\omega_e P_g - \frac{R_g}{L_g}Q_g + \frac{3}{2L_g}U_{Qg}$$

$$U_{Qg} = \frac{2L_g}{3}\left(\frac{dQ_g}{dt} + \frac{R_g}{L_g}Q_g\right) + \omega_e P_g * \frac{2L_g}{3}$$

Let, $k_{Qg} = \frac{2L_g}{3}$

$$\therefore U_{Qg} = K\left(\frac{dQ_g}{dt} + \frac{R_g}{L_g}Q_g\right) + K\omega_e P_g$$

Let,

$$\sigma_{Qg} = \frac{dQ_g}{dt} + \frac{R_g}{L_g}Q_g = k_{Qg}\left(Q_g^* - Q_g\right)$$

$$\therefore k_{Qg}Q_g^* = \left(\frac{d}{dt} + \frac{R_g}{L_g} + k_{Qg}\right)Q_g$$

$$\frac{Q_g}{Q_g^*} = \frac{k_{Qg}}{p + \frac{R_g}{L_g} + k_{Qg}} = \frac{k_{QgP} + \frac{k_{Qg}i}{p}}{p + \frac{R_g}{pL_g} + k_{Qgp} + \frac{k_{Qg}i}{p}}$$

$$\frac{Q_g}{Q_g^*} = \frac{k_{QgP}\left(1 + \frac{k_{Qg}i}{pk_{Qgp}}\right)}{p\left(1 + \frac{R_g}{pL_g}\right) + k_{Qgp}\left(1 + \frac{k_{Qg}i}{pk_{Qgp}}\right)}$$

$$Let, \frac{R_g}{pL_g} = \frac{k_{Qg}i}{pk_{Qgp}} \rightarrow k_{Qg}i = \frac{R_g}{L_g}k_{Qgp} \qquad (60)$$

$$\frac{Q_g}{Q_g^*} = \frac{k_{Qgp}}{p + k_{Qgp}}$$

$$pole = -k_{Qgp} \quad and, \; \alpha = k_{Qgp}$$

$$\therefore k_{Qg}i = \frac{R_g}{L_g}\alpha \& k_{Qgp} = \alpha \qquad (61)$$

C. DC LINK VOLTAGE CONTROLLER DESIGN

In this subsection, the DC link voltage controller ensures fast and proper control of the GSC instantaneous active and reactive power. For PI controller design, let;

$$\sigma_v = \frac{C_{dc}}{2}pv_{dc}^2 = k_v(v_{dc}^{*2} - v_{dc}^2) \qquad (62)$$

From (62), the dc link model transfer function is obtained as follows:

$$\frac{v_{dc}^2}{v_{dc}^{*2}} = \frac{k_v}{\frac{C_{dc}}{2}p + k_v} = \frac{1}{1 + \frac{C_{dc}}{2k_v}p} \qquad (63)$$
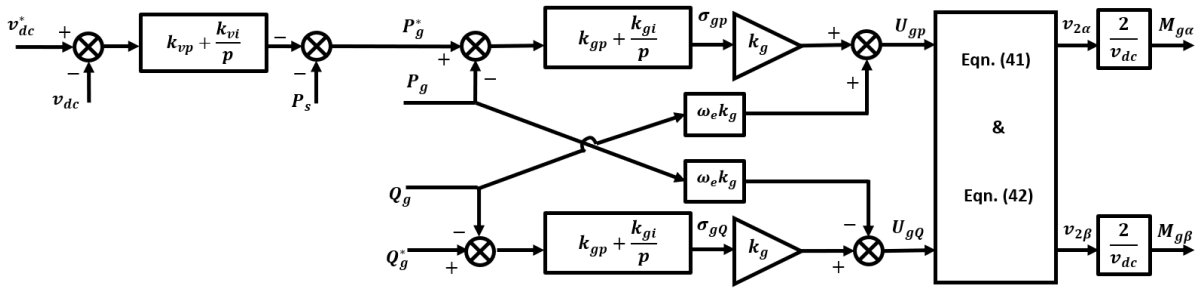
FIGURE 5. GSC-DPC controller design for constant DC link voltage control and regulation of the power injected into the electric network.

From (63), poles $= -\frac{2k_v}{C_{dc}}$ and bandwidth:

$$\alpha = \frac{2k_v}{C_{dc}} \qquad (64)$$

where

$$k_v = \frac{C_{dc}}{2}\alpha \equiv k_{vp} + \frac{k_{vi}}{p}$$

$$k_{vp} = \frac{C_{dc}}{2}\alpha \quad \text{and} \quad k_{vi} = 0$$

Also, the controller parameters are shown in Table 2.

TABLE 2. System parameters.

k_{wP}	31.4159	k_{wi}	0
k_{PsP}	628.32	k_{Psi}	4494.9
k_{QsP}	628.32	k_{Qsi}	4494.9
k_{dcP}	10	k_{dci}	0
k_{PgP}	167.88	k_{Pgi}	6999.63
k_{QgP}	167.88	k_{Qgi}	6999.63

V. STABILITY ANALYSIS

Network parameters can significantly impact the stability of an SPMSG system connected to any electric network. Therefore, this section presents how changes in MSC and GSC impedance, DC link capacitance, and rotor speed affect the stability and dynamic response of the electric network under investigation. The electric network stiffness at a particular node can be characterized by either (1) inertia or/and (2) impedance of the system seen from the corresponding connection point that is inversely proportional to the SCR [35], [36]. A strong AC network is characterized by a small impedance (high SCR), and a weak AC network by a high impedance and, therefore, a low SCR at any particular node, e.g., PCC. According to the literature, AC nodes with SCR<3 are considered weak connection points [37]. SCR is calculated as the ratio of the electric network's short-circuit capacity at the PCC to the rated power of the wind turbine, which is expressed in [38] as:

$$SCR = \frac{v_{pcc,\,nom}^2}{P_{t,\,rated}\,|Z_g|} \qquad (65)$$

By increasing the electric network impedance in (65), the proposed electric network connected SPMSG dynamic

performance under stiff and weak-electric network conditions can be evaluated. To gain a better understanding of the proposed system's stability, a reduced-order small-signal model [39], has been used to analyze Fig. 1. The corresponding system input dynamic state and coefficient matrix are provided in equations (66) and (67), respectively. The eigenvalues, which can be calculated by manipulating equation (67), indicate the system's stability based on their distribution.

$$\left[pP_s \, pQ_s \, pv_{dc}^2 \, pP_g \, pQ_g \right]' \qquad (66)$$

$$\begin{bmatrix} -\frac{R}{L} & (\frac{\omega_r L_s}{L} + s\omega_e) & 0 & 0 & 0 \\ -(\frac{\omega_r L_s}{L} + s\omega_e) & -\frac{R}{L} & 0 & 0 & 0 \\ -\frac{1}{C_{dc}} & 0 & -\frac{1}{C_{dc}} & 0 & 0 \\ 0 & 0 & 0 & -\frac{R_g}{L_g} & \omega_e \\ 0 & 0 & 0 & -\omega_e & -\frac{R_g}{L_g} \end{bmatrix}$$

$$(67)$$

VI. RESULTS AND DISCUSSIONS

To examine the viability and dynamic performance of the proposed DPC model, a specific 30kW SPMSG has been modeled and implemented in MATLAB/SIMULINK software. An OWT is used to drive the SPMSG rotor at zero pitch angle, and the resulting stator out power is connected to the electric network through a full AC-DC-AC converter.

A. PROPOSED MSC-DPC AND GSC-DPC STEADY-STATE AND TRANSIENT PERFORMANCE

The steady-state and transient response of the proposed DPC-based electric network-connected SPMSG system control is compared with the conventional VCC shown in Fig. 2. The outer loop controller model has a bandwidth of 500Hz, while the inner loop has double times higher bandwidth, which is calculated in reference to equations (47), (51), (56), (59), (61) and (64). The average wind speed is initially set to 6 m/s during the simulation and then changes to 10 m/s at 4 sec to examine the transient dynamics of the system. Fig. 6 shows the controlled rotor speed (w_r) and electromagnetic torque (T_e) performance of the two different control models to sudden wind speed (V_w) step-change. The results show that the DPC controller has a faster transient response than

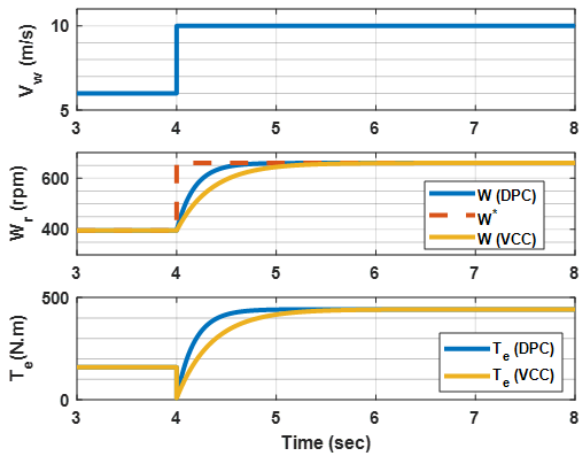**FIGURE 6.** Controlled rotor speed and electromagnetic torque dynamic response to sudden wind speed step-change.
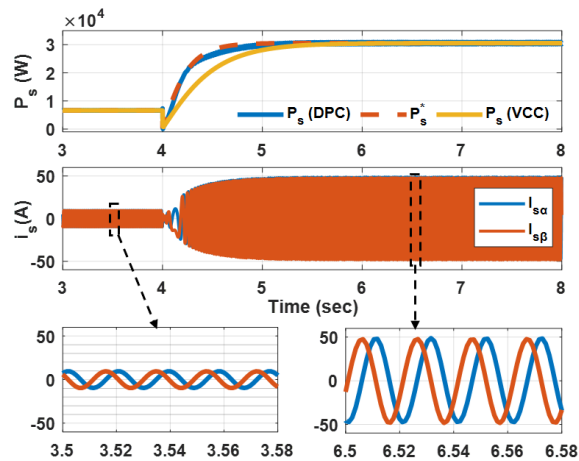

FIGURE 7. Controlled SPMSG stator active power and current dynamic response to sudden wind speed step-change at unity pf.

FIGURE 8. Controlled GSC output dynamic response to sudden wind speed step-change at unity pf.

the traditional VCC method. It can be inferred that the MSC-DPC generator rotor speed followed the reference dynamic response more closely, even after the transient dynamic test when the rotor speed suddenly changed from 400 rpm to 720 rpm at 4 sec simulation time. This sudden change necessitated a ramping action that caused the VCC controller more time to track the reference than DPC method. Also, the DPC T_e showed a faster response when compared to the VCC counterpart. Figure 7 illustrates the controlled SPMSG stator output active power and $\alpha\beta$-current operating at unity power factor (pf), which also changed in relation to the wind speed at MPPT. The results indicate that the MSC-DPC's decoupled active power exhibits a faster response compared to the active power of the VCC method.

Fig. 8 compares the GSC power output between the proposed DPC model and the VCC method. The transient response results show that the sudden step-change in wind speed at 4.0 sec simulation time impacted the VCC method more adversely. Additionally, it can be seen from the decoupled GSC-DPC $\alpha\beta$-current that the sudden change in wind
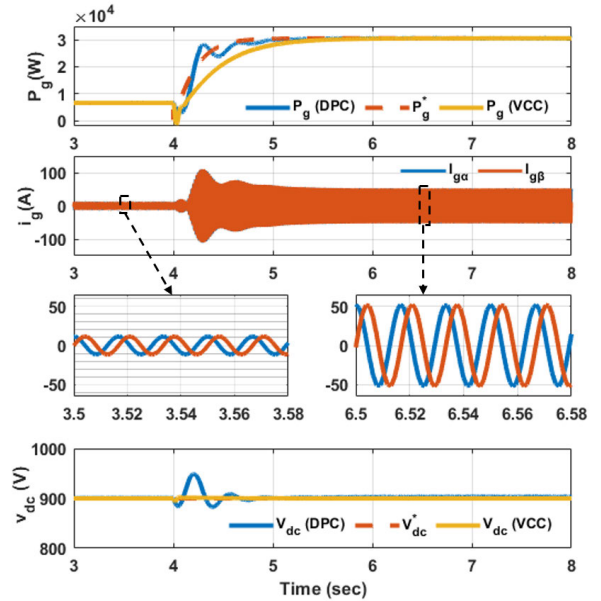
speed had minimal effect on current injection into the electric network. The performance of the designed GSC-DPC controller in providing a fast response to maintain a constant DC link voltage is also shown in Fig. 8. The average wind speed sudden step-change had minimal impact on the DC link voltage magnitude, with only a small swell observed during the sudden change of rotor speed from 400 rpm to 720 rpm at 4 sec, which settled within 0.5 sec. Overall, it is not readily apparent that there are significant differences in the steady-state performance of both methods for sudden step change in SPMSG rotor speed.

B. PERFORMANCE OF THE PROPOSED MSC-DPC AND GSC-DPC UNDER DIFFERENT WIND SPEED

To provide a more thorough analysis of the proposed model, a simulation was conducted to evaluate the control performance of the proposed MSC-DPC and GSC-DPC dynamics at different wind speeds, both in high and low regions. The simulation results are presented in Figs. 9 and 10. During the simulation, the SPMSG is operating at unity pf, and the average wind speed available to the turbine changes from 7 m/s to 5 m/s and vice versa in steps of 1 m/s, and the system operation is evaluated.

Fig. 9 shows the MSC electromagnetic torque and current response to different wind speed levels, and it is observed that the controlled current response to the average wind speed changes is adequate. The response exhibited minimal overshoot, and the transient recovery rate is fast in relation to the reference value. Moreover, from the decoupled MSC-DPC active and reactive power dynamics, it is observed that the proposed method's transient response and steady-state performance are not significantly affected by the variations
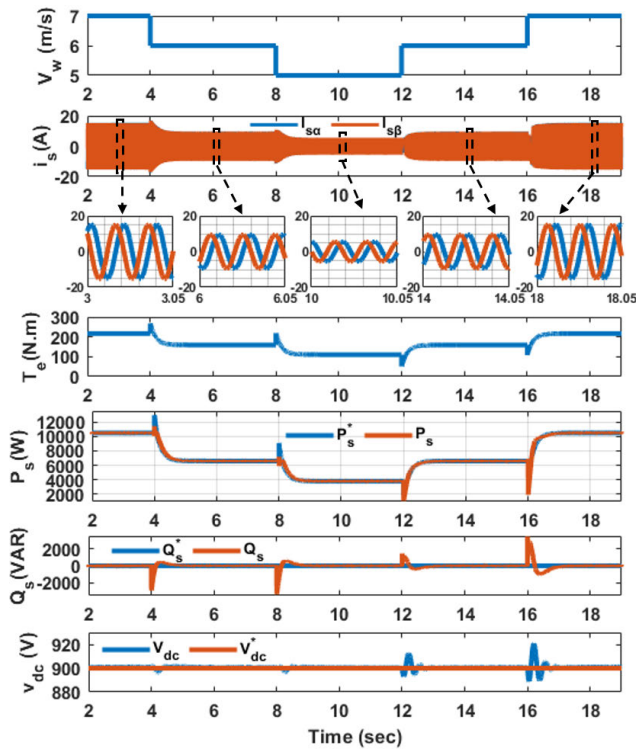
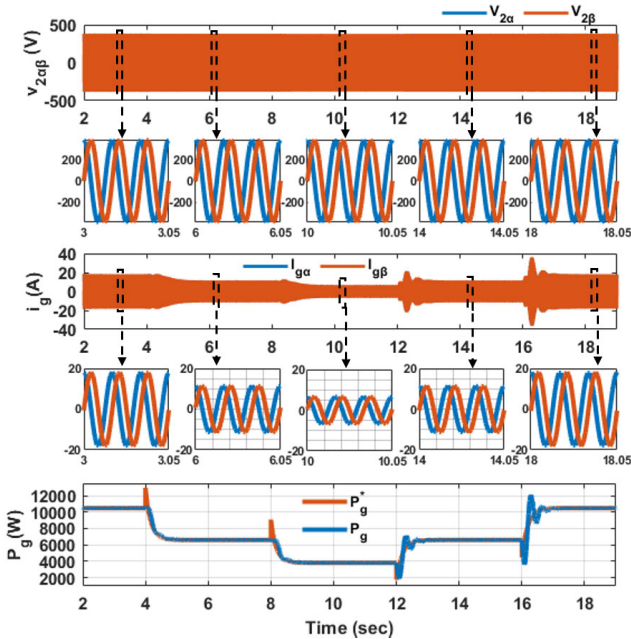**FIGURE 9.** MSC-DPC and DC link voltage performance under varying wind speed.

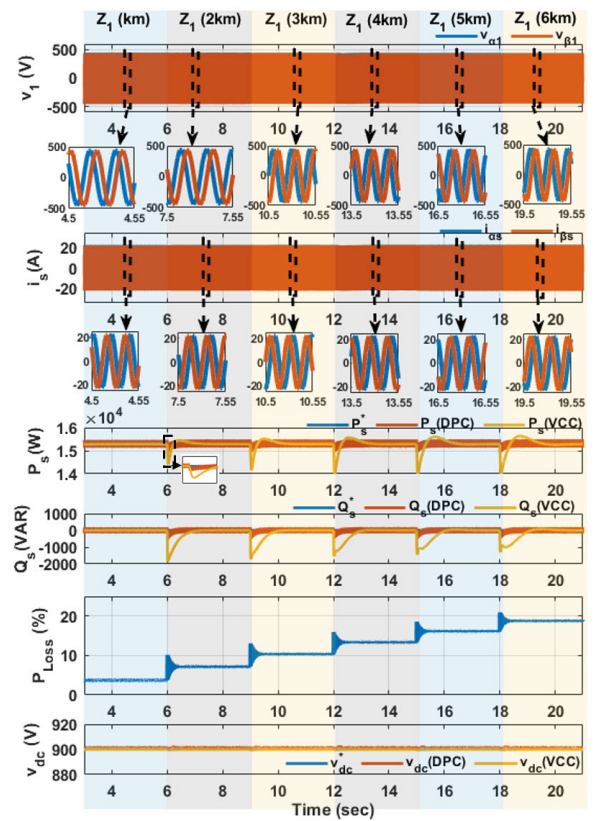**FIGURE 10.** GSC-DPC performance under varying wind speed.

FIGURE 11. MSC-DPC performance under different coupling MSC line length.

show that the electric network injected current and power response changed in proportion with the variations in wind speed, while the PCC voltage ($v_{2\alpha\beta}$) remained fairly constant. The decoupled active power, operating at the unity power factor, exhibited a rapid transient recovery, even in the face of sudden wind speed fluctuations.

Overall, the simulation results demonstrated the satisfactory performance of the proposed MSC-DPC and GSC-DPC dynamics in adapting to wind speed variations and maintaining proper power output.

C. PERFORMANCE OF THE PROPOSED DPC UNDER DIFFERENT COUPLING MSC LINE LENGTHS

To assess the control performance of the proposed DPC for various MSC coupling conductor lengths, a simulation is conducted, as depicted in Fig. 11. Given that the proposed model entails removing the BTB-converter from the turbine's nacelle and situating it at a specific distance (either onshore or within the deck of an oil or gas rig platform, depending on the application), the coupling MSC line impedance is increased per km in 3-second simulation time steps at an average wind speed of 8 m/s.

By evaluating the enlarged MSC voltage and current dynamic results, it is apparent that the proposed method's transient response and steady-state performance remain relatively unaffected by an increase in line distance up to 6 km.

in available wind speed. Furthermore, the transient dynamic overshoot of the DC link voltage on speed step changes is due to the power flow transients on the GSC side.

The corresponding effect of varying wind speed step changes on the GSC-DPC is presented in Fig. 10. The results

The transient dynamics of the injected active and reactive power suggest that the proposed DPC model delivers superior performance and remains unaffected by changes in MSC coupling impedance, in contrast to the VCC model, which is significantly influenced. Moreover, the power loss percentage per line km increment demonstrates that extending the line length beyond 3 km would result in considerable power loss above 10%. The DC link voltage performance also responded satisfactorily to line variations for both DPC and VCC models.
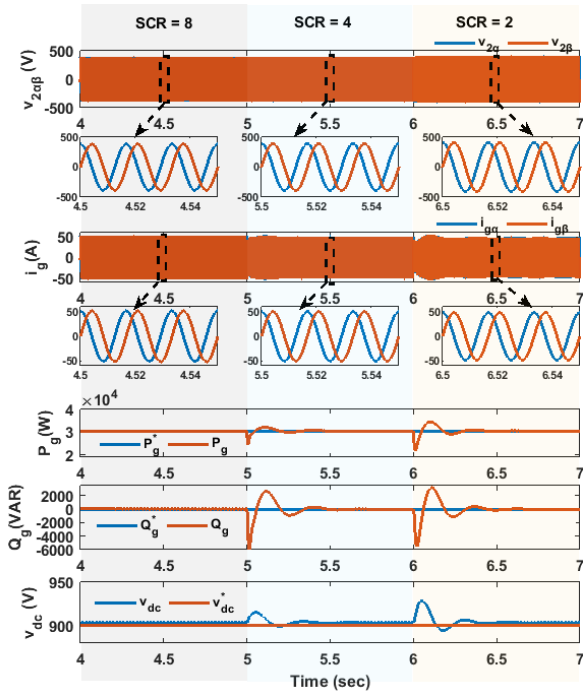
FIGURE 12. Performance of the proposed DPC SPMSG system under different electric network SCR values.

FIGURE 13. Eigenvalues of the system as rotor speed $0 \leq w_r \leq 377$ rad/s.

FIGURE 14. Eigenvalues of the system as MSC coupling impedance Z_1 increases with length 1 km $\leq l \leq$ 20 km.

D. PERFORMANCE OF THE PROPOSED DPC TO ELECTRIC NETWORK PARAMETER CHANGES

The control performance of the proposed DPC scheme for the SPMSG system is evaluated under varying SCR values, as shown in Fig. 12. At the start of the simulation; the SPMSG is connected to a stiff electric network with an SCR value of 8. After 5 seconds, the electric network impedance doubles, reducing the SCR to 4. Following that, at 6 seconds, the SCR value is further decreased to 2, representing a weak electrical network. From the simulation results, it is clear that operating the wind turbine when connected to a weaker strength system (SCR = 2) leads to higher magnitude transient oscillations in the injected active and reactive power and the BTB-converter dc-link voltage. This happens due to the increased voltage sensitivity at DPC-GSC at PCC when the SCR decreases, which in turn adversely affects the performance of various control loops in the BTB-converter control system. However, the results show satisfactory steady-state performance despite the varying SCR values, demonstrating the effectiveness of
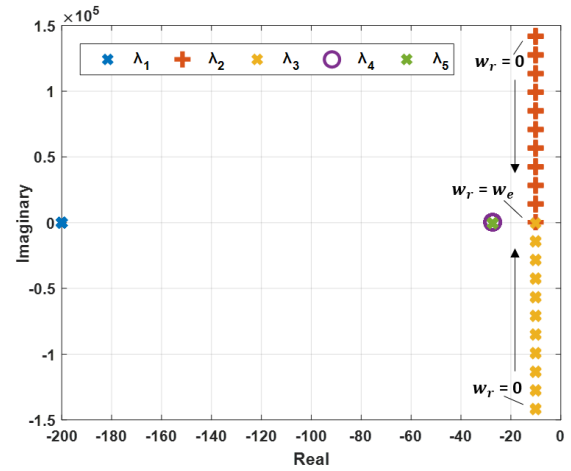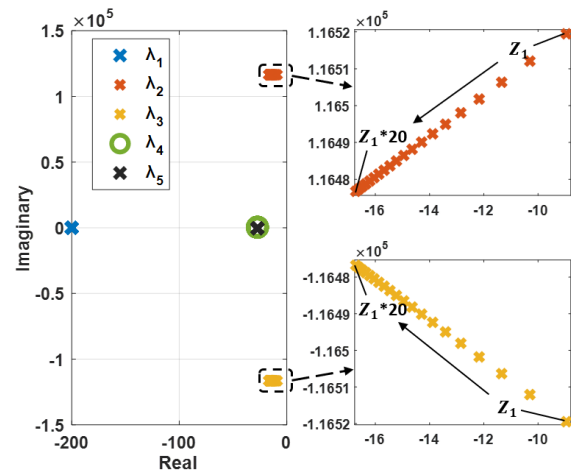
the proposed DPC approach. The robustness of the OWT-SPMSG system is investigated in the next section.

E. STABILITY ANALYSIS RESULTS

In this subsection, an eigenvalue analysis of (67) is presented to demonstrate the stability of the proposed model under varying system parameters. Fig. 13 shows the distribution of the system's eigenvalues as rotor angular speed is increased from zero to the gird-rated angular frequency value. It is observed that the conjugate pairs that dominate the distribution of the eigenvalues moved closer to zero. This implies that operating the SPMSG w_r close to the electric network w_e value increases the system stability profile. Fig. 14 presents the impact of increasing the impedance of the short-distance line connecting the offshore SPMSG to the onshore converter. The result shows that the dominant eigenvalues conjugate pair moved farther away from the origin as the line distance increased from 1 to 20 km. This result is consistent with the dynamic analysis shown in Fig. 11, which showed a longer settling time as line distance increases.
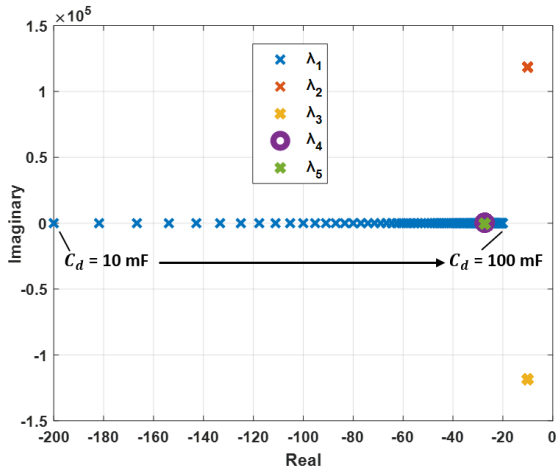
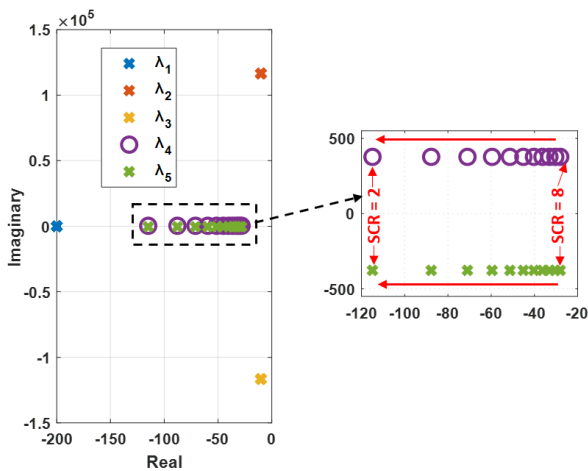**FIGURE 15.** Eigenvalues of the system as GSC coupling DC link capacitance increases 10 mF $\leq C_{dc} \leq$ 100 mF.

FIGURE 16. Eigenvalues of the system as electric network SCR changes from stiff to weak electric network ($2 \leq SCR \leq 8$).

Additionally, Fig. 15 shows how variations in C_{dc} value affect the system's eigenvalues distribution. It is observed that the dominant eigenvalue moved closer to the origin as C_{dc} value increased to 10 times its rated value, leading to increased system stability. Fig. 16 shows the impact of increasing electric network impedance, such that the SCR value decreases from 8 to 2. It can be observed that the dominant eigenvalues conjugate pair moves further away from the origin as the SCR decreases. However, in general, the eigenvalues are located in the left half-plane, suggesting that the proposed wind turbine-connected SPMSG technology and control structure can produce a suitable performance for a wide range of system conditions, particularly weak systems of the future.

F. DISCUSSION
The proposed DPC method for an electric network-connected SPMSG wind turbine has been simulated under different conditions. The steady-state performance of the DPC has been compared with that of the traditional VCC

method, which has the same control bandwidth. Overall, the simulation results demonstrate that similar steady-state performance is exhibited by the proposed DPC method as the VCC. Furthermore, a fast transient response is exhibited by the DPC method in controlling the SPMSG electromagnetic torque and active power under varying rotor speeds. Additionally, the proposed DPC is shown to be robust against variations in system parameter conditions and works well under weak electric network conditions.

However, the accuracy of the proposed method can be influenced by any current offset errors, leading to periodic ripples in the controlled electromagnetic torque and power during the transient state [40], which can result in degraded system performance. Additionally, any unbalanced current can introduce negative sequence components and second-order harmonics in the stator currents [41], decreasing steady-state performance. Dual-sequence controllers and compensation terms can be implemented in the control loops to mitigate these issues, as suggested in [42] and [43]. However, exploring the impact of unbalanced voltage and grid-side faults on SPMSG direct power control is beyond the scope of this paper and requires further discussion. Notably, implementing field-weakening control strategies could mitigate the inherent drawback of SPMSGs, i.e., insignificant reluctance torque generation, and improve the system stability at high rotor speeds [44].

VII. CONCLUSION
This paper considers OWT-SPMSG system direct power control as an effective method for offshore applications. The OWT is located offshore and connected to the electric network through a short-distance line and full BTB-converter. This arrangement is anticipated to reduce the construction and maintenance costs of the OWT infrastructure. Unlike the conventional VCC method, the proposed DPC uses Clarke's transformation, feed-forward, and PI control structures to ensure effective instantaneous power control. The system dynamic models are used to design the MSC, DC link, and GSC controllers. The approach is straightforward to implement and does not require complex calculations for reference current or fine-tuned inner current control loops. Simulation results demonstrate that the proposed method extracts the maximum available wind power and ensures power delivery at unity power factor to the electric network. Additionally, the eigenvalue stability analysis results indicate that the proposed model maintains stability in response to variations in system parameters, which may occur due to different operating conditions, including stiff and weak electrical network conditions. Future research may focus on developing a sequence DPC-SPMSG controller to investigate its performance during electric network fault events.

REFERENCES
[1] A. Follo, O. Saborío-Romano, E. Tedeschi, and N. A. Cutululis, "Challenges in all-DC offshore wind power plants," *Energies*, vol. 14, no. 19, p. 6057, Sep. 2021.

[2] P. Catalán, Y. Wang, J. Arza, and Z. Chen, "A comprehensive overview of power converter applied in high-power wind turbine: Key challenges and potential solutions," *IEEE Trans. Power Electron.*, vol. 38, no. 5, pp. 6169–6195, May 2023, doi: 10.1109/TPEL.2023.3234221.

[3] G. Stewart and M. Muskulus, "A review and comparison of floating offshore wind turbine model experiments," *Energy Proc.*, vol. 94, pp. 227–231, Jan. 2016.

[4] S. M. Mortensen, K. Laugesen, J. K. Jensen, K. Jessen, and M. Soltani, "Experimental verification of the hydro-elastic model of a scaled floating offshore wind turbine," in *Proc. IEEE Conf. Control Technol. Appl. (CCTA)*, Copenhagen, Denmark, Aug. 2018, pp. 1623–1630, doi: 10.1109/CCTA.2018.8511565.

[5] M. A. Soliman, H. M. Hasanien, H. Z. Azazi, E. E. El-Kholy, and S. A. Mahmoud, "An adaptive fuzzy logic control strategy for performance enhancement of a grid-connected PMSG-based wind turbine," *IEEE Trans. Ind. Informat.*, vol. 15, no. 6, pp. 3163–3173, Jun. 2019, doi: 10.1109/TII.2018.2875922.

[6] Z. Xinghua and C. Pengfei, "Efficiency optimization of direct torque controlled interior permanent magnet synchronous motor considering iron losses," in *Proc. 19th Int. Conf. Electr. Mach. Syst. (ICEMS)*, Nov. 2016, pp. 1–5.

[7] S. Kumari, V. Kushwaha, and T. N. Gupta, "A maximum power point tracking for a PMSG based variable speed wind energy conversion system," in *Proc. Int. Conf. Power Energy, Environ. Intell. Control (PEEIC)*, Apr. 2018, pp. 789–794.

[8] J. Li, X. Wang, J. Lyu, H. Zong, T. Xue, Z. Fang, and X. Cai, "Stability analysis of wind farm connected to hybrid HVDC converter," in *Proc. IEEE 9th Int. Power Electron. Motion Control Conf. (IPEMC-ECCE Asia)*, Nanjing, China, Nov. 2020, pp. 3258–3262, doi: 10.1109/IPEMC-ECCEAsia48364.2020.9367833.

[9] A. Youssef, E. E. M. Mohamed, and A. I. M. Ali, "Model predictive control for grid-tie wind-energy conversion system based PMSG," in *Proc. Int. Conf. Innov. Trends Comput. Eng. (ITCE)*, Feb. 2018, pp. 467–472.

[10] J. Dong, Y. Huang, L. Jin, and H. Lin, "Comparative study of surface-mounted and interior permanent-magnet motors for high-speed applications," *IEEE Trans. Appl. Supercond.*, vol. 26, no. 4, pp. 1–4, Jun. 2016, doi: 10.1109/TASC.2016.2514342.

[11] Y. Wang, H. Wang, W. Liu, and Q. Wang, "Modeling and analysis of a new voltage regulation method for surface-mounted permanent magnet synchronous generator," in *Proc. IEEE 18th Int. Power Electron. Motion Control Conf. (PEMC)*, Budapest, Hungary, Aug. 2018, pp. 574–579, doi: 10.1109/EPEPEMC.2018.8521986.

[12] C. He and T. Wu, "Analysis and design of surface permanent magnet synchronous motor and generator," *CES Trans. Electr. Mach. Syst.*, vol. 3, no. 1, pp. 94–100, Mar. 2019, doi: 10.30941/CESTEMS.2019.00013.

[13] L. He, Y. Li, and R. G. Harley, "Adaptive multi-mode power control of a direct-drive PM wind generation system in a microgrid," *IEEE J. Emerg. Sel. Topics Power Electron.*, vol. 1, no. 4, pp. 217–225, Dec. 2013.

[14] Y. Belkhier and A. Y. Achour, "Passivity-based current control strategy for PMSG wind turbine," in *Proc. 1st Int. Conf. Sustain. Renew. Energy Syst. Appl. (ICSRESA)*, Dec. 2019, pp. 1–4.

[15] Z. Zhang, Z. Cui, Z. Zhang, R. Kennel, and J. Rodríguez, "Advanced control strategies for back-to-back power converter PMSG wind turbine systems," in *Proc. IEEE Int. Symp. Predictive Control Electr. Drives Power Electron. (PRECEDE)*, May 2019, pp. 1–6, doi: 10.1109/PRECEDE.2019.8753366.

[16] H. Gashtil, V. Pickert, D. Atkinson, D. Giaouris, and M. Dahidah, "Comparative evaluation of field oriented control and direct torque control methodologies in field weakening regions for interior permanent magnet machines," in *Proc. IEEE 13th Int. Conf. Compat., Power Electron. Power Eng. (CPE-POWERENG)*, Apr. 2019, pp. 1–6.

[17] S. Bose, Md. R. Islam, T. Islam, and Md. A. Rafiq, "Fuzzy logic based sensorless adaptive direct torque control of surface permanent magnet synchronous motor (SPMSM) drives," in *Proc. 3rd Int. Conf. Electr. Inf. Commun. Technol. (EICT)*, Dec. 2017, pp. 1–5, doi: 10.1109/EICT.2017.8275175.

[18] B. D. Lemma and S. Pradabane, "Control of permanent-magnet synchronous motors using fuzzy logic considering parameter variation and diagnostic capability for hostile environment applications," in *Proc. IEEE 1st Int. Conf. Smart Technol. Power, Energy Control (STPEC)*, Sep. 2020, pp. 1–4.

[19] F. Z. H. Pacha, W. Amri, N. Fezai, and A. Benamor, "Intelligent control based on adaptative fuzzy logic for permanent magnet synchronous machine," in *Proc. 4th Int. Conf. Adv. Syst. Emergent Technol.*, Dec. 2020, pp. 124–129, doi: 10.1109/IC_ASET49463.2020.9318278.

[20] M. Ahmed, M. Abdelrahem, I. Harbi, and R. Kennel, "Evaluation of predictive direct current and direct power control for grid-connected PV systems," in *Proc. 5th IEEE Workshop Electron. Grid (eGRID)*, Nov. 2020, pp. 1–6, doi: 10.1109/eGRID48559.2020.9330637.

[21] H. Karimi-Davijani and O. Ojo, "Optimum control of grid connected interior permanent magnet wind turbine generator," in *Proc. IEEE Energy Convers. Congr. Expo. (ECCE)*, Sep. 2012, pp. 3764–3771.

[22] Y. Gui, X. Wang, F. Blaabjerg, and D. Pan, "Control of grid-connected voltage-source converters: The relationship between direct-power control and vector-current control," *IEEE Ind. Electron. Mag.*, vol. 13, no. 2, pp. 31–40, Jun. 2019, doi: 10.1109/MIE.2019.2898012.

[23] D. Dong, B. Wen, D. Boroyevich, P. Mattavelli, and Y. Xue, "Analysis of phase-locked loop low-frequency stability in three-phase grid-connected power converters considering impedance interactions," *IEEE Trans. Ind. Electron.*, vol. 62, no. 1, pp. 310–321, Jan. 2015, doi: 10.1109/TIE.2014.2334665.

[24] X. Wang and F. Blaabjerg, "Harmonic stability in power electronic-based power systems: Concept, modeling, and analysis," *IEEE Trans. Smart Grid*, vol. 10, no. 3, pp. 2858–2870, May 2019, doi: 10.1109/TSG.2018.2812712.

[25] Y. Gui, J. D. Bendtsen, and J. Stoustrup, "Sliding mode control with grid voltage modulated direct power control for three-phase AC–DC converter," in *Proc. Chin. Control Conf. (CCC)*, Jul. 2019, pp. 7436–7441, doi: 10.23919/ChiCC.2019.8865280.

[26] Y. Gui, C. Kim, C. C. Chung, J. M. Guerrero, Y. Guan, and J. C. Vasquez, "Improved direct power control for grid-connected voltage source converters," *IEEE Trans. Ind. Electron.*, vol. 65, no. 10, pp. 8041–8051, Oct. 2018.

[27] A. Jabbarnejad and S. Vaez-Zadeh, "Power quality improvement using virtual flux combined control of grid connected converters under balanced and unbalanced grid operation," in *Proc. 45th Annu. Conf. IEEE Ind. Electron. Soc.*, vol. 1, Oct. 2019, pp. 6166–6171, doi: 10.1109/IECON.2019.8927653.

[28] S. Gao, H. Zhao, Y. Gui, D. Zhou, and F. Blaabjerg, "An improved direct power control for doubly fed induction generator," *IEEE Trans. Power Electron.*, vol. 36, no. 4, pp. 4672–4685, Apr. 2021.

[29] (Feb. 17, 2021). *Consortium Develops Wind-Powered Offshore Desalination System*. Accessed: Mar. 29, 2023. [Online] https://www.offshore-mag.com/renewable-energy/article/14197799/consortium-develops-windpowered-offshore-desalination-system

[30] *Power Management Options for Offshore Oil & Gas Rigs*. Accessed: Mar. 30, 2023. [Online]. Available: https://www.wpowerproducts.com/news/how-to-power-offshore-oil-rigs/

[31] *SD3EX Offshore Wind Turbine*. SD Wind Energy. Accessed: Mar. 30, 2023. [Online]. Available: https://sd-windenergy.com/small-wind-turbines/sd3ex-3kw-offshore-wind-turbines/

[32] Y. Gui, X. Wang, and F. Blaabjerg, "Vector current control derived from direct power control for grid-connected inverters," *IEEE Trans. Power Electron.*, vol. 34, no. 9, pp. 9224–9235, Sep. 2019, doi: 10.1109/TPEL.2018.2883507.

[33] A. Egea-Alvarez, S. Fekriasl, F. Hassan, and O. Gomis-Bellmunt, "Advanced vector control for voltage source converters connected to weak grids," *IEEE Trans. Power Syst.*, vol. 30, no. 6, pp. 3072–3081, Nov. 2015, doi: 10.1109/TPWRS.2014.2384596.

[34] Y. Ma, L. Yang, J. Wang, F. Wang, and L. M. Tolbert, "Emulating full-converter wind turbine by a single converter in a multiple converter based emulation system," in *Proc. IEEE Appl. Power Electron. Conf. Expo.*, Mar. 2014, pp. 3042–3047.

[35] *IEEE Guide for Planning DC Links Terminating at AC Locations Having Low Short-Circuit Capacities*, IEEE Standard 1204–1997, 1997.

[36] D. Yang, X. Wang, F. Liu, K. Xin, Y. Liu, and F. Blaabjerg, "Adaptive reactive power control of PV power plants for improved power transfer capability under ultra-weak grid conditions," *IEEE Trans. Smart Grid*, vol. 10, no. 2, pp. 1269–1279, Mar. 2019, doi: 10.1109/TSG.2017.2762332.

[37] P. Kundur, *Power System Stability and Control*. New York, NY, USA: McGraw-Hill, 1994.

[38] L. Zhang, L. Harnefors, and H.-P. Nee, "Interconnection of two very weak AC systems by VSC-HVDC links using power-synchronization control," *IEEE Trans. Power Syst.*, vol. 26, no. 1, pp. 344–355, Feb. 2011, doi: 10.1109/TPWRS.2010.2047875.

[39] W. Du, Z. Chen, K. P. Schneider, R. H. Lasseter, S. P. Nandanoori, F. K. Tuffner, and S. Kundu, "A comparative study of two widely used grid-forming droop controls on microgrid small-signal stability," *IEEE J. Emerg. Sel. Topics Power Electron.*, vol. 8, no. 2, pp. 963–975, Jun. 2020.

[40] S. Lee, H. Kim, and K. Lee, "Current measurement offset error compensation in vector-controlled SPMSM drive systems," *IEEE J. Emerg. Sel. Topics Power Electron.*, vol. 10, no. 2, pp. 2619–2628, Apr. 2022, doi: 10.1109/JESTPE.2022.3151351.

[41] H.-S. Jung, S.-H. Hwang, J.-M. Kim, C.-U. Kim, and C. Choi, "Diminution of current-measurement error for vector-controlled AC motor drives," *IEEE Trans. Ind. Appl.*, vol. 42, no. 5, pp. 1249–1256, Sep. 2006, doi: 10.1109/TIA.2006.880904.

[42] S. Zhou, J. Liu, L. Zhou, and H. She, "Dual sequence current controller without current sequence decomposition implemented on DSRF for unbalanced grid voltage conditions," in *Proc. IEEE Energy Convers. Congr. Expo. (ECCE)*, Sep. 2014, pp. 60–67, doi: 10.1109/ECCE.2014.6953376.

[43] D. D. S. Mota, E. F. Alves, and E. Tedeschi, "Dual sequence controller with delayed signal cancellation in the rotating reference frame," in *Proc. IEEE 22nd Workshop Control Model. Power Electron. (COMPEL)*, Nov. 2021, pp. 1–8, doi: 10.1109/COMPEL52922.2021.9646023.

[44] Y. Shen, H. Wang, Y. Wang, W. Liu, and L. Wu, "A novel field-weakening control method of SPMSG based on single current regulator," in *Proc. 25th Int. Conf. Electr. Mach. Syst. (ICEMS)*, Nov. 2022, pp. 1–5, doi: 10.1109/ICEMS56177.2022.9983065.

SATISH M. MAHAJAN (Life Senior Member, IEEE) received the B.E. degree in electrical engineering from the University of Poona, Pune, India, in 1978, the M.S. degree in electrical engineering from The State University of New York at Buffalo, Buffalo, NY, USA, in 1983, and the Ph.D. degree in electrical engineering from the University of South Carolina, Columbia, SC, USA, in 1987.

Since 1987, he has been the Faculty of the Department of Electrical and Computer Engineering, Tennessee Technological University (TTU), Cookeville, TN, USA. He is currently the Director of the Center for Energy Systems Research (CESR), TTU. His current research interests include the physical phenomena of optoelectronic and HV devices and the modeling of conventional and renewable power systems.

CHIKEZIE M. EMEGHARA (Student Member, IEEE) received the B.Eng. degree (Hons.) in electrical electronic engineering from Anambra State University, Nigeria, in 2011, and the M.Eng. degree from the Michael Okpara University of Agriculture, Umudike, Nigeria, in 2017. He is currently pursuing the Ph.D. degree in electrical and computer engineering with Tennessee Technological University, Cookeville, TN, USA.

He has more than five years of working experience in a power distribution company and more than three years of research experience with the Center for Energy Systems Research, Tennessee Technological University.

ALI ARZANI (Member, IEEE) received the M.Sc. degree in electric power engineering from the Royal Institute of Technology (KTH), Sweden, and the Ph.D. degree in electrical engineering from Clemson University, USA, with a focus on power and energy systems. He was a Visiting Researcher with the ABB Corporate Research Center, Sweden, and a Lecturer with Azad University (IAU). Currently, he is a Research Assistant Professor of electrical engineering with the Center for Energy Systems Research (CESR), Tennessee Technological University, USA. His current research interests include renewable energy systems operation and control in active distribution and transmission networks and technologies pertaining to smart grid.

● ● ●